



OPEN ACCESS

EDITED BY

Fan Yang,
Lanzhou University, China

REVIEWED BY

Hua-Wen Cao,
China Geological Survey, China
Xiaoqiang Zhu,
Anhui Normal University, China
Yi-Qu Xiong,
Central South University, China

*CORRESPONDENCE

Chang-Hao Xiao,
xiaochanghao1986@126.com

†These authors have contributed equally to this work and share first authorship

SPECIALTY SECTION

This article was submitted to Economic Geology, a section of the journal Frontiers in Earth Science

RECEIVED 30 August 2022

ACCEPTED 31 October 2022

PUBLISHED 09 January 2023


CITATION

Xiao C-H, Yu P-P, Liu X-H, Liu X-C, Tang Y-W, Wang W-L and Zhang Y (2023), Cassiterite U-Pb dating and micro-XRF analysis constraint on the formation of Xinlu Sn-Zn deposit, South China.
Front. Earth Sci. 10:1031681.
doi: 10.3389/feart.2022.1031681

COPYRIGHT

© 2023 Xiao, Yu, Liu, Liu, Tang, Wang and Zhang. This is an open-access article distributed under the terms of the [Creative Commons Attribution License \(CC BY\)](https://creativecommons.org/licenses/by/4.0/). The use, distribution or reproduction in other forums is permitted, provided the original author(s) and the copyright owner(s) are credited and that the original publication in this journal is cited, in accordance with accepted academic practice. No use, distribution or reproduction is permitted which does not comply with these terms.

Cassiterite U-Pb dating and micro-XRF analysis constraint on the formation of Xinlu Sn-Zn deposit, South China

Chang-Hao Xiao ^{1,2*†}, Ping-Ping Yu^{1,2†}, Xiao-Hu Liu³, Xiang-Chong Liu^{1,2}, Yan-Wen Tang⁴, Wen-Lei Wang^{1,2} and Yu Zhang⁵

¹Laboratory of Dynamic Diagenesis and Metallogenesis, Institute of Geomechanics, Chinese Academy of Geological Sciences, Beijing, China, ²Key Laboratory of Paleomagnetism and Tectonic Reconstruction, Ministry of Natural Resources, Beijing, China, ³College of Earth Sciences, Guilin University of Technology, Guilin, China, ⁴Stake Key Laboratory of Ore Deposit Geochemistry, Institute of Geochemistry, Chinese Academy of Sciences, Guiyang, China, ⁵School of Earth Sciences and Resources, China University of Geosciences, Beijing, China

This study presents rock slab and thin section reflection mapping, element mapping by Micro-XRF (μ -XRF) analysis, and *in situ* cassiterite U-Pb laser ablation-inductively coupled plasma mass spectrometer (LA-ICP-MS) ages of the Xinlu Sn-Zn deposit, Nanling Sn-W belt, South China. The new results provided constraints on the age and processes of Sn mineralization and thus further discussed the role of the Paleo-Pacific plate in the formation of Sn-W mineralization in the Nanling Sn-W belt. Based on mineralogy and μ -XRF analysis, four mineralization episodes are distinguished in the Baimianshan segment, Xinlu deposit, including 1) prograde skarn stage characterized by the mineral assemblages of garnet, pyroxene, marble, hornfels; 2) retrograde skarn-sulfide composed of massive pyrrhotite, sphalerite with parts of epidote, cassiterite; 3) quartz sulfide vein stage consisting of arsenopyrite, pyrite, quartz, and 4) barren calcite crosscutting the former episodes. The time of retrograde skarn-sulfide mineralization is dated by LA-ICP-MS cassiterite U-Pb at 168.7 ± 1.3 Ma. These U-Pb ages, combined with previous geochronological studies, support one Sn mineralization event associated with the 159.5–168.7 Ma magmatism in the Guposhan-Huashan district. The Xinlu Sn-Zn mineralization and the Middle-Late Jurassic Sn-W mineralization in the Nanling belt, South China is genetically related to asthenospheric upwelling and crust-mantle interaction caused by the subduction of the Paleo-Pacific plate. Our results demonstrate that thin section reflection and μ -XRF element mapping are powerful tools for determining paragenesis in ore deposits and are highly effective to guide the selection of analytical positions for cassiterite U-Pb dating. This method may also be applicable to *in-situ* geochronology of other minerals.

KEYWORDS

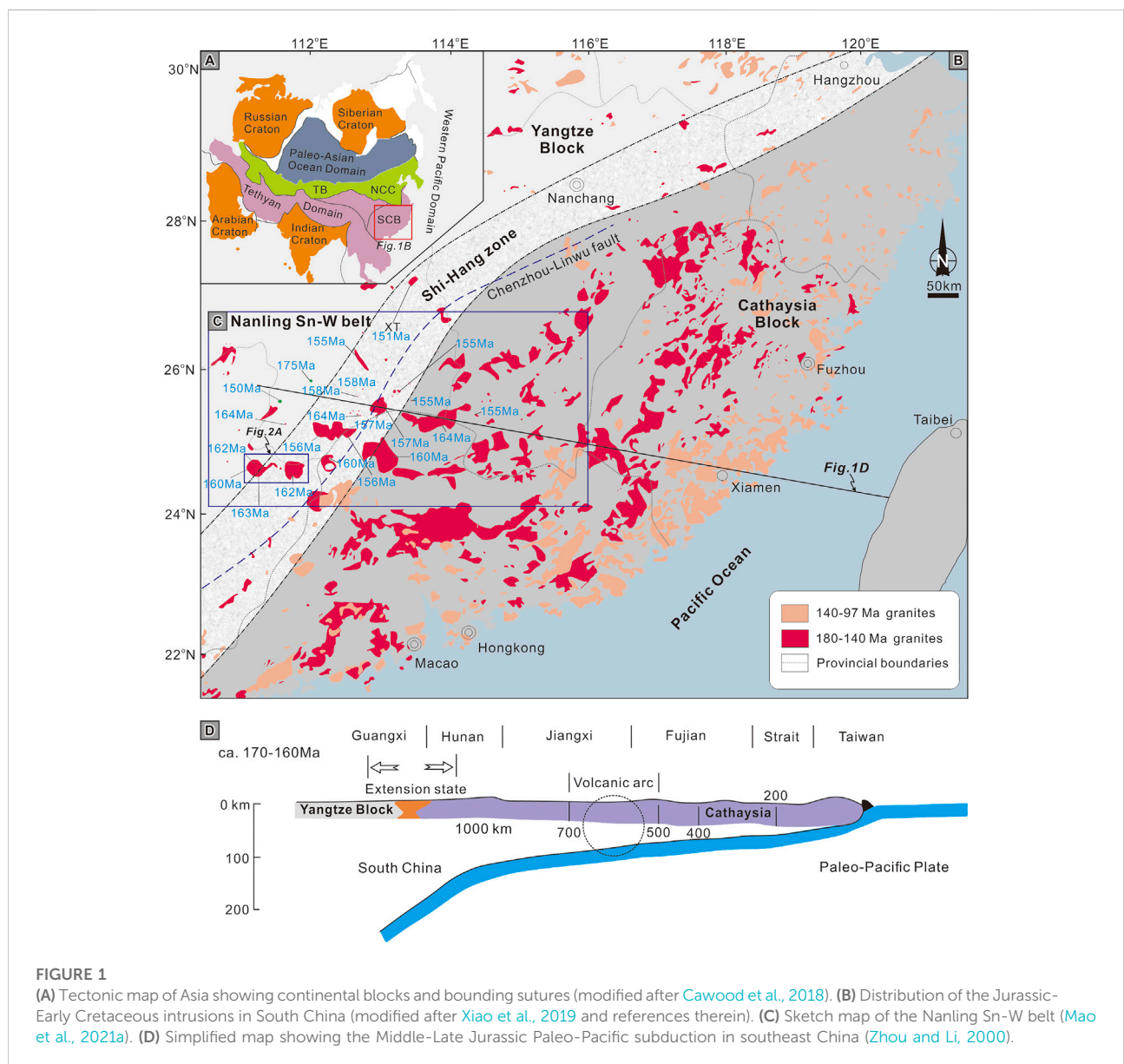
micro-XRF, Xinlu deposit, Nanling Sn-W belt, South China, Paleo-Pacific, cassiterite U-Pb geochronology

Introduction

The Nanling Sn-W belt is a world-class Sn and W province within the South China Block (SCB) (Figures 1A,B; Mao et al., 2021b). Most tungsten and tin deposits are related to the late Jurassic felsic rocks (Xiao et al., 2019; Mao et al., 2021a). The spatial distribution of these rocks displays a southeastward younging trend (Figure 1C), which was interpreted to be related to the flat-slab subduction of the Paleo-Pacific Ocean plate (Figure 1D; Li and Li, 2007; Yang et al., 2020). In contrast, the Sn-W mineralization in this region does not display a similar age pattern. The ore-forming ages of most of large-scale W and Sn deposits in the Nanling Sn-W belt concentrated in 160–150 Ma. Therefore, whether the Paleo-Pacific plate

contributed to the formation of Sn-W mineralization is equivocal.

Cassiterite U-Pb dating has proved to be a robust method to precisely and directly date the tin mineralization of W-Sn deposits (Yuan et al., 2008; Zhang et al., 2015; Xiao et al., 2022). Most published cassiterite U-Pb dating required mineral separation and grain mounts. A major drawback of these two methods is that they may mix polygenetic populations of cassiterite. Hence, the rapid identification of cassiterite on the hand specimen or thin section before the cassiterite U-Pb dating is quite essential. Micro-XRF analyses are a powerful and non-destructive technique to determine the trace elements in the geological samples, and to identify the minerals and their contents (Flude et al., 2017; Wang et al., 2022).



Above all, the μ -XRF analyses have great potential to guide the selection of analytical spots for cassiterite U-Pb dating.

The Guposhan-Huashan Sn-W district is one of the most important districts in the western of the Nanling Sn-W belt (Figure 1C). The Sn-W deposits in this district (e.g., Xinlu Sn-Zn deposit, Shuiyanba Sn deposit, Keda Sn deposit, Huashan Sn deposit, and Shanhu W-Sn deposit) are located at the contact zone of the Guposhan-Huashan granite pluton and its vicinity (Figures 1C, 2A; Feng et al., 2019; Gu et al., 2007a, b; Kang et al., 2012; Li et al., 2016; Xiao et al., 2011; Zhang et al., 2020; Zhao et al., 2010). Considerable uncertainty and controversy remains regarding the exact timing of W-Sn mineralization. For example, some studies revealed that no direct genetic link between Sn-W mineralization in the Xinlu deposit and the Guposhan pluton based on whole-rock K-Ar ages and fluid inclusion Rb-Sr ages of the ores (Dong, 1991; Zhu et al., 2006; Gu et al., 2007a). Many researchers have demonstrated that W-Sn mineralization was related to the Guposhan pluton based on zircon U-Pb, molybdenite Re-Os, and muscovite/biotite Ar-Ar dating results in the Xinlu deposit (Kang et al., 2012; Li et al., 2016; Feng et al., 2019). Besides, molybdenite, with Re-Os ages representing the ore-forming ages, is not a major mineral in the Xinlu deposit, and most other tested minerals could not be directly dated for ore-forming ages (Feng et al., 2019). Thirdly, the skarn Sn-Zn mineralization with great economic values lacks investigation compared to the abundant studies on the quartz vein type Sn-W mineralization. All these lead to the ambiguous timing of the tin mineralization in the Guposhan-Huashan Sn-W district.

In this contribution, we applied microscopic observation and μ -XRF analysis to determine the paragenetic sequence and cassiterite occurrence in the Xinlu deposit. We performed laser ablation-inductively coupled plasma-mass spectrometry (LA-ICP-MS) U-Pb dating of cassiterite to directly date tin mineralization. From our new cassiterite U-Pb age, and previously published cassiterite U-Pb ages, we refined the spatial and temporal distribution of Sn-W mineralization and discussed the role of the Paleo-Pacific plate in the formation of Sn-W mineralization in the Nanling Sn-W belt.

Geological setting

Regional geology

The South China Block is composed of the Yangtze Block in the northwest and the Cathaysia Block in the southeast (Figure 1B). These two blocks were welded along the “Shi-Hang zone” during the Early Neoproterozoic, which was a tectonic-granitoid belt (Figure 1B; Gilder et al., 1996). The SCB subsequently underwent the Early Paleozoic NS shortening intraplate tectono-magmatism (Shu et al., 2021), the Triassic intraplate orogeny (Li et al., 2022), and the Late

Mesozoic tectonic transformation (Shu, 2012). Large-scale Sn-W mineralization events occurred during the Mesozoic in the eastern SCB. Numerous studies have demonstrated that the subduction of the Paleo-Pacific plate was responsible for producing large-scale magmatism and Sn-W mineralization (Li and Li, 2007; Mao et al., 2021a, b; Zhou and Li, 2000).

The Nanling Sn-W belt locates in the central south of the SCB. In this belt, there are intensive folded and deformed basement, magmatic rocks, and rifting basins (Zhang et al., 2015). The basement is composed of a metamorphosed Neoproterozoic-Ordovician flysch-volcanic series, covered by unmetamorphosed Late Devonian to Early Triassic sedimentary rocks. Five episodic magmatism events (Neoproterozoic, Silurian, Permian, Triassic, Jurassic, and Cretaceous) occurred in this belt (Zhang et al., 2015). Previous studies indicate that W and Sn mineralization occurred in the belt in the Neoproterozoic and Mesozoic (Figure 1C; Hu and Zhou, 2012), of which the latter is economically more important.

This study focuses on the Guposhan-Huashan W-Sn district in the western of the Nanling Sn-W belt, which is located in the eastern of the Guangxi Zhuang Autonomous Region (GZAR). The study area mainly consists of semipelagic flysch sedimentary rocks and subsequently underwent the Early Paleozoic intraplate orogeny. Scattered Mo-W, Pb-Zn, and Au mineralization associated with this orogeny are represented by the Baishiding, Zhanggongling, and Longshui deposits in the eastern of the district (Figure 2A; Li et al., 2016). From Early Devonian to Jurassic, carbonate platforms with sporadic clastic rocks formed in this area under a shore-shallow sea-slope setting (Shu, 2012). The Jurassic clastic rocks, formed in a graben basin, unconformably overly the Paleozoic rocks (Figure 2A). Large-scale magmatism and associated Sn-W mineralization occurred in response to the subduction of the Pacific plate in the Middle-Late Jurassic and Cretaceous (Figure 2A; Feng et al., 2019; Gu et al., 2007a; Gu et al., 2007b; Kang et al., 2012; Li et al., 2016; Xiao et al., 2011; Zhang et al., 2020; Zhao et al., 2010). The Quaternary system hosts alluvial tin, which is widely distributed in the south of the district. Folds and faults are widely developed in this district.

Ore deposit geology

The Xinlu Sn-Zn deposit is located at the south contact zone of the Guposhan granite pluton and its vicinity. It consists of the Shihuichong Sn-Fe, Xinlu Sn-Zn, Liuheao Sn, Muqiaomian Sn-Zn, Baimianshan Sn-Zn, and Shimen Sn-Zn segments from north to south (Figure 2B). The main sedimentary rocks in the deposit are composed of middle Devonian Xindu Formation (D_{2x}) and Yujiang Formation (D_{2y}) clastic rocks, Donggangling Formation (D_{2d}) carbonate rocks, upper Devonian Guilin (D_{3g}) and Rongxian (D_{3r}) formations, and

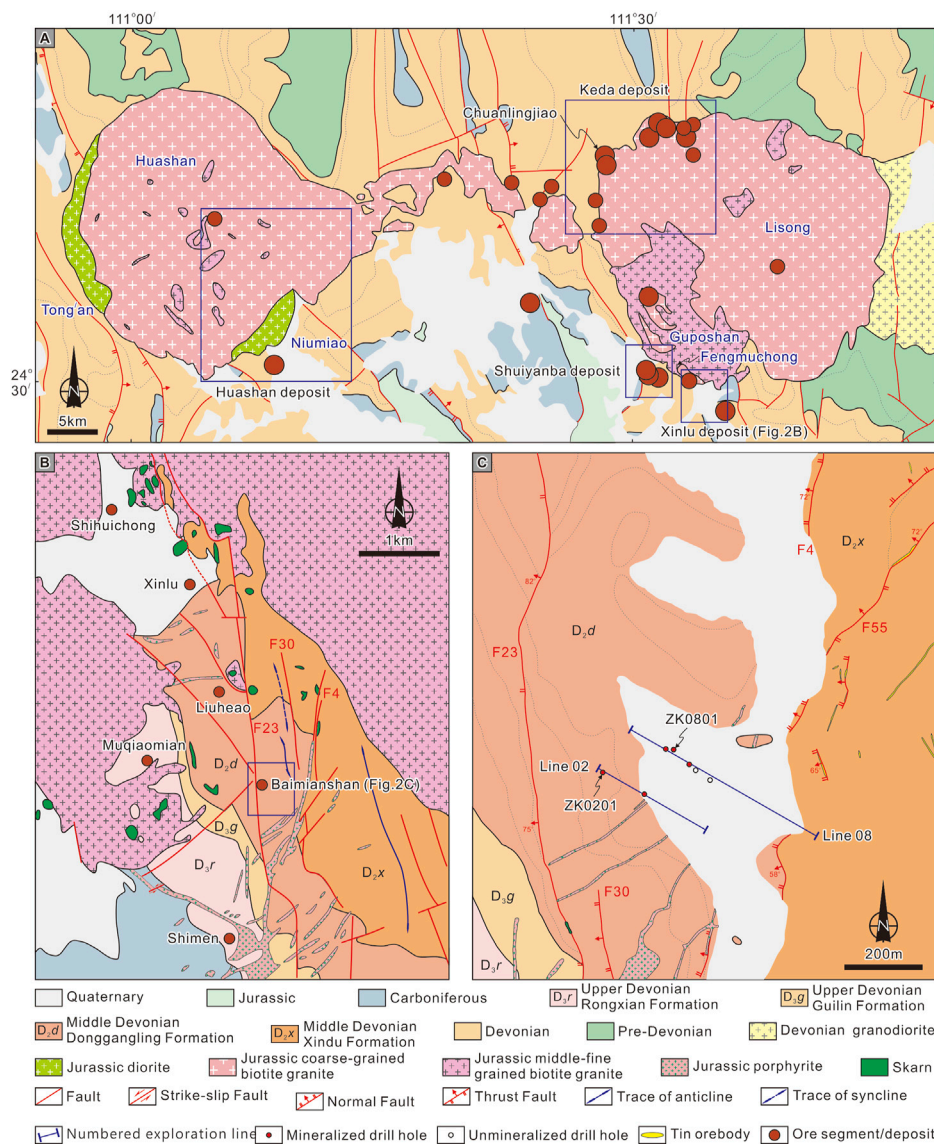
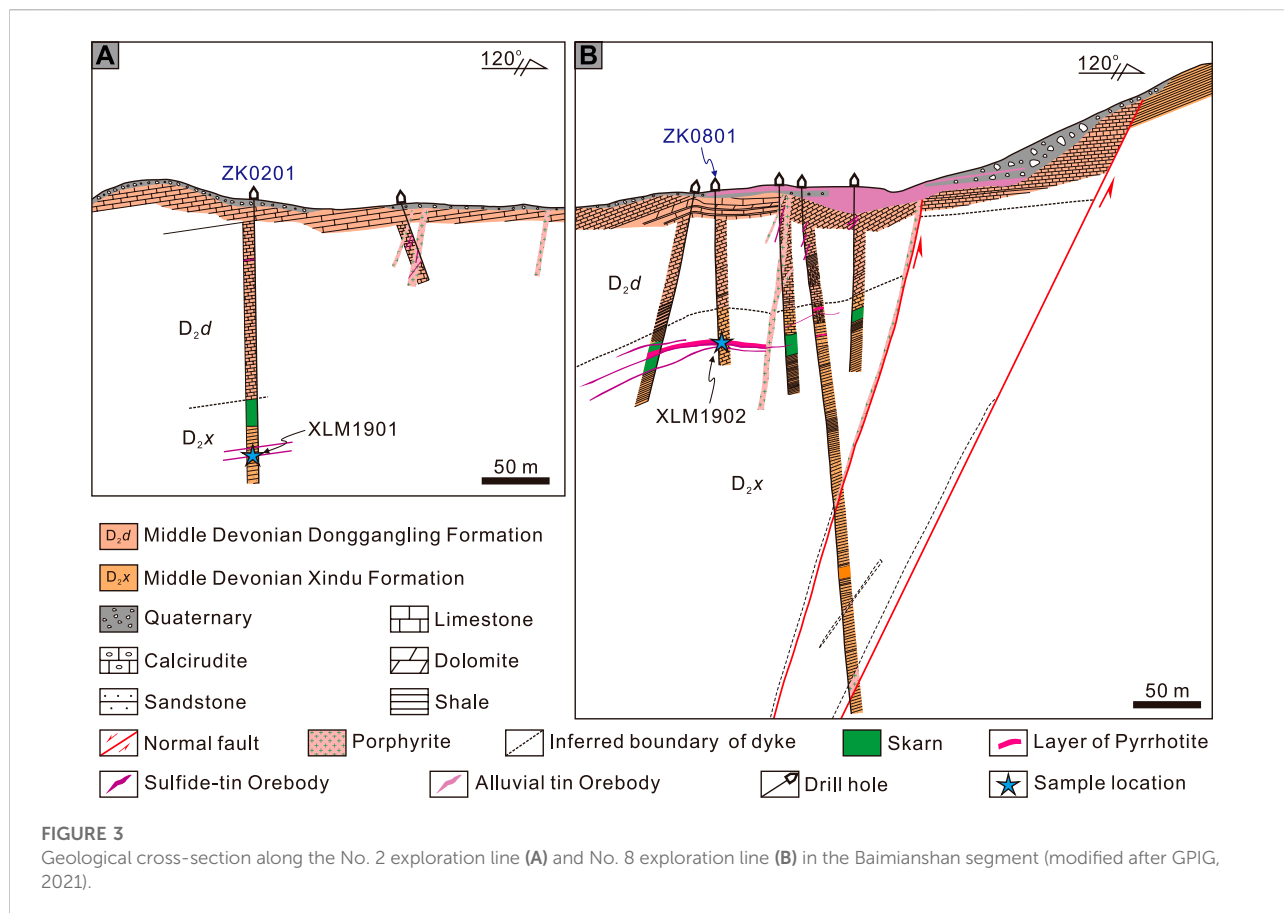


FIGURE 2 (A) Geological map of Guposhan-Huashan Sn-W district (modified after Geological Prospecting Institute of Guangxi (GPIG), 2021). (B) Geological map of Xinlu Sn-Zn deposit (modified after Feng et al., 2019). (C) Geological map of Baimianshan Zn-Sn segment (modified after GPIG, 2021).

Lower Carboniferous carbonate rocks. The NNW-, NW-, NE-, and EW-striking faults are widely developed in the deposit. The NNW-striking faults control the distribution of major ore segments in the deposit (Figure 2B). The dextral EW-striking faults crosscut the NNW-, and NW-striking faults. The NNW-striking faults plunge to the directions of 260°–290° at dip angles of 58°–85°. Most of the NE-striking faults plunge in the directions of 330°–340° at angles of 72°–85°. Fault-parallel folds are developed in the southeastern of the deposit. The Guposhan granite is distributed in the northern half of the deposit. Minor intermediate-felsic dykes are distributed along or crosscut the

NE-, and NW-striking faults in the southern part of the deposit. Minor skarn and fault-controlled oxidized orebodies crop out on the surface in the deposit (Figure 2C).

The Baimianshan Sn-Zn segment is controlled by the NNW-striking normal faults (F₂₃) and is located in the middle of the Xinlu deposit (Figures 2B,C). The carbonate rocks of the Donggangling Formation and clastic rocks of the Xindu Formation are distributed on the east and west sides of the segments, respectively. The Devonian system developed in the west limb of the Kejiashan anticline and the stratum dipped SWW at 12°–30° (Hu et al., 1992). The Quaternary sediments



unconformably overly the Devonian in the middle of the segment. The NS-striking F_{23} and F_4 normal faults vertical cross throughout the segment. Previous studies revealed that these NS-striking faults underwent nearly E–W compression following an E–W extension (Ou, 1989). The main NE-trending concealed orebody was formed between these two faults. Parts of oxidized orebodies were formed along the NE-, and small NS-striking faults in the eastern of the segment. Most of the NE-striking faults are normal faults except for the F_{55} fault. A few of NS-, and NE-striking dykes spread in the south of the segment. The alteration is not developed on the surface, and it includes silicification, potassic alteration, and sericitization. Some small skarn is found in the F_{23} fault. The orebodies are mainly buried underground with insignificant oxidized ore exposed on the surface.

Sampling and analytical methods

The hand specimens in this study were collected from drill cores ZK0201 and ZK0801 from two of the new holes of the Baimianshan segment in 2019 (Figures 3, 4). The two drill

cores have ferrous-sphalerite-cassiterite sulfide orebodies at the lithological contacts in the upper of the Xindu Formation (D_{2x}) with a small number of sulfide orebodies in the Donggangling Formation (D_{2d}) limestone. Two types of ores including XLM1901 and XLM1902 were sampled. Sample XLM1901 is massive ferrous sphalerite-cassiterite-arsenopyrite sulfide that was formed in the Donggangling Formation limestone at 49.64 m of drill hole ZK0201. The Sn and Zn ore grades of XLM1901 are 0.31% and 8.65%, respectively. Sample XLM1902 is a layer-parallel skarn cassiterite sulfide orebody that was formed in the upper part of the Xindu Formation at 133 m of drill hole ZK0801 with 2.46% Sn and 2.04% Zn. The ore was formed in the contacts between pellet marlstone and argillaceous siltstone. We carried out observation on 10 hand specimens, micro-observation, reflection mapping, and μ -XRF analysis on 2 representative polished slabs and 1 polished thin section, and cathodoluminescence (CL) imaging of targeted cassiterite grains, and LA-ICP-MS dating to obtain detailed paragenesis and cassiterite U–Pb ages of the Baimianshan segment, Xinlu deposit.



FIGURE 4

Photographs of representative ore and rocks within the Baimianshan Zn-Sn segment. (A) Core from drill hole ZK0801. (B) Massive garnet and marble were crosscut by steep-dipping calcite veins. (C) Steep-dipping branching veins or veinlets and layer-parallel massive ores overlying on the layer-parallel marble and hornfels. (D) Steep-dipping pyrite-quartz-calcite veins crosscut the marble. (E) The arsenopyrite replaced the massive pyrrhotite-chalcocopyrite-sphalerite and both were crosscut by the pyrite-quartz-calcite veins. (F) Massive pyrrhotite-chalcocopyrite-sphalerite ore.

Thin section reflection mapping and element mapping by μ -XRF

Sample XLM1901 is a 6.5*6.5 cm² half drill core piece and XLM1902 is a cylindrical rock chip of 6.8 cm in diameter and 1.6 cm in height. The analytical areas included the whole surface of the polished slabs and thin sections for petrographic observations and element mapping. Polished sections and slabs were examined using transmitted and reflected optical microscopes (DM4500P, Leica, Germany). Reflection mapping of the whole polished slabs on the microscope was completed by manual splicing through Image Analysis System software (Figures 5A,B). The μ -XRF analyses on rock slabs and thin sections were performed on the benchtop M4 Tornado (Bruker, Germany) under vacuum conditions (20 mbar, 50 kV, 200 μ A) with a diameter of 20 μ m X-ray beam with 40 μ m pixel size. Element mapping scanning and sample navigation on the benchtop M4 were run by a motorized stage that moves the sample beneath the static X-ray beam. Data were collected for Fe, Zn, W, Ga, Ge, As, Pb, Bi, Sn, Cu, W, Si, Al, Ca, and S (Figures 6–8). The analytical procedures of element mapping were described in detail by Flude et al. (2017) and Wang et al. (2022). These

analyses were conducted at the Laboratory of Dynamic Diagenesis and Metallogenesis, Institute of Geomechanics, Chinese Academy of Geological Science (LDDM-IGM, CAGS). All data acquisition and processing were carried out using the proprietary Bruker software supplied with the instrument.

Cassiterite U-Pb dating and cathodoluminescence imaging

Based on the microscopic observation and μ -XRF analysis, we mixed the two samples to separate cassiterite grains at the LDDM-IGM, CAGS. And then, the cassiterite was mounted on epoxy resin discs. Cassiterite grains were observed under the microscope, and CL and BSE images were obtained to characterize the texture of cassiterite and avoid cracks and mineral/fluid inclusions before U-Pb dating. Selected cassiterite domains without any obvious mineral inclusion were analyzed for U-Pb ages using the Agilent 7900 LA-ICP-MS at the State Key Laboratory of Ore Deposit Geochemistry, Institute of Geochemistry, Chinese Academy of Sciences. Cassiterite grains have a core-rim microstructure, and

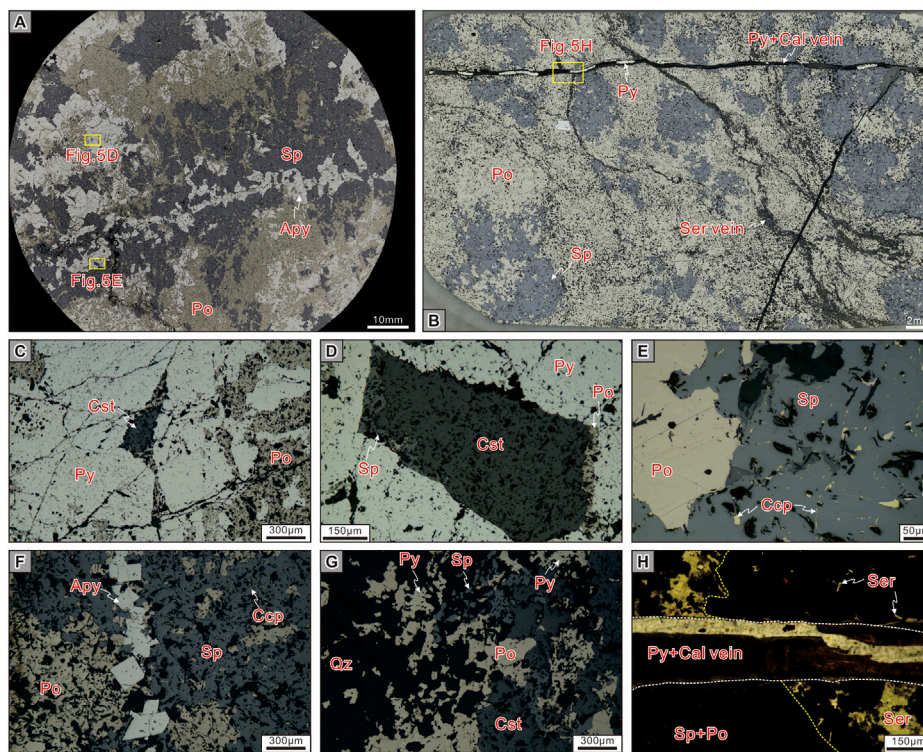


FIGURE 5

Representative textures and mineral assemblages within ores and wall rocks of Baimianshan Zn-Sn segment. (A) The reflected mapping of polished slab of XLM1902. (B) The reflected mapping of thin section XLM1901T showing the pyrite vein replaced the massive pyrrhotite-sphalerite. (C–D) Cassiterite coexisted with arsenian pyrite and replaced by the pyrrhotite, sphalerite. (E) The pyrrhotite laths and lamellae, chalcopyrite blebs intergrown with sphalerite and pyrrhotite. (F) The euhedral arsenopyrite quartz veinlet crosscut the pyrrhotite and sphalerite. (G) The pyrite quartz replaced the sphalerite and pyrrhotite. (H) The pyrite-calcite vein cut the massive pyrrhotite and sphalerite which were replaced sericite.

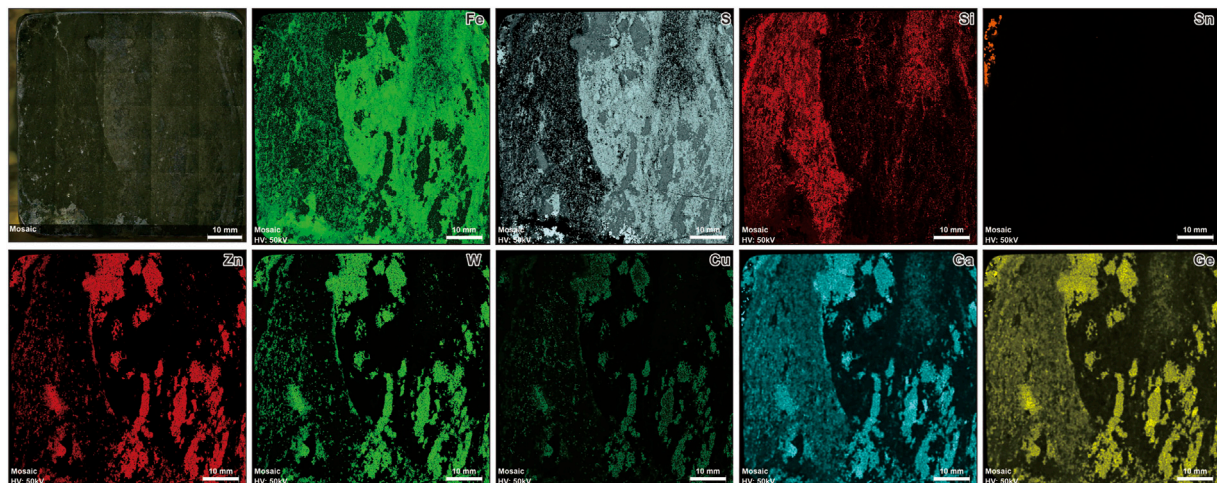


FIGURE 6

Photograph and corresponding μ -XRF single-element maps (Fe, S, Si, Sn, Zn, W, Cu, Ga, Ge) of rock slab XLM1901.

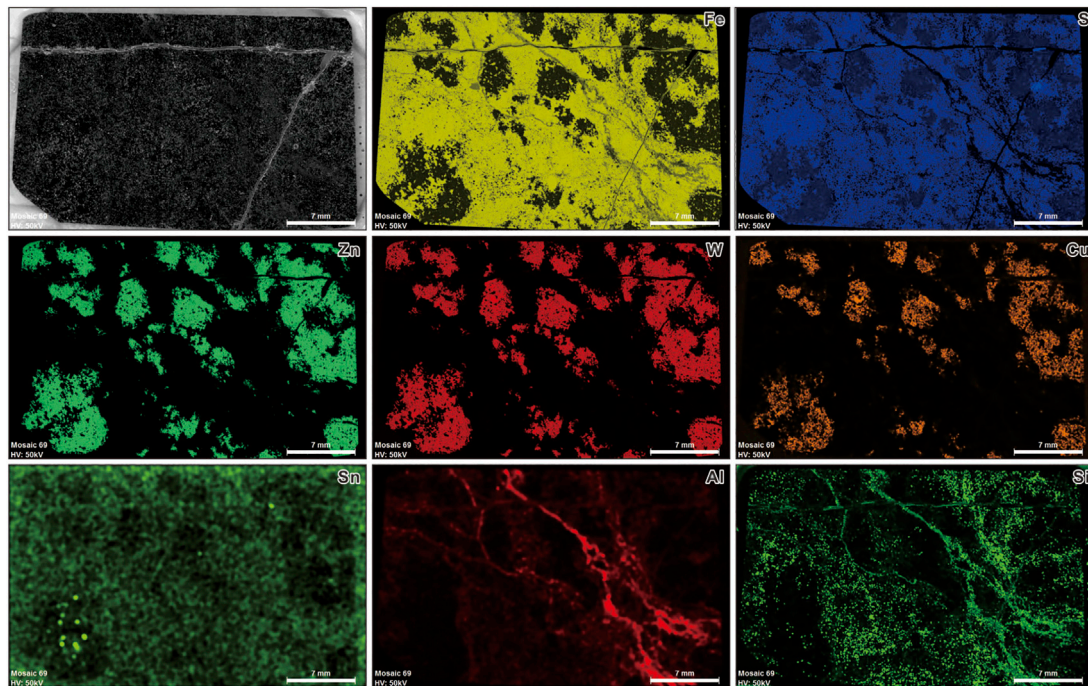


FIGURE 7
Photograph and single-element μ -XRF maps (Fe, S, Zn, W, Cu, Sn, Al, Si) of thin section XLM1901T.

thirty spots including 17 fully-dark cores and 13 gray oscillatory rims were analyzed. The reference materials used were AY-4 cassiterite for $^{206}\text{Pb}/^{238}\text{U}$ ratios (ID-TIMS U-Pb age of 158.2 ± 0.4 Ma; Yuan et al., 2008) and NIST SRM 612 for U, Th, and Pb concentrations of cassiterite.

Cassiterite grains were analyzed using LA-ICP-MS with a laser energy density of $5 \text{ J}/\text{cm}^2$, a spot size of $60 \mu\text{m}$, and a repetition rate of 6 Hz. NIST SRM 612 was analyzed twice and AY-4 was analyzed three times for every ten analyses of the unknown cassiterite grains. Each spot analysis incorporated a background signal acquisition of approximately 20 s followed by 35 s of sample data acquisition. Other conditions were listed by Tang et al. (2022). The uncertainty of the single population, ratio uncertainty of the AY-4 reference material, and decay constant uncertainties were propagated to the final results during the process of offline raw data reduction by ICPMSDataCal (Liu et al., 2008). Data errors for isotopic ratios in the cassiterite samples are 1σ . Isoplot 3.0 was used to calculate the U–Pb ages and draw Concordia diagrams (Ludwig, 2003).

Results

Mineralogy and paragenesis

According to the field observation, the Baimianshan segment is similar to most Zn skarn deposits which occur distal from the

causative pluton (Meinert et al., 2005). Most ores on drilling cores are present as massive with minor skarn minerals or hosted by veins and veinlets with skarn alteration halos (Figure 4). Based on microscopic observations, the mineralization process of the Baimianshan segment could be divided into prograde skarn (stage I), retrograde skarn-sulfide (stage II), quartz sulfide veins (stage III), and barren carbonate (stage IV) stages. The prograde stage is characterized by the mineral assemblages of garnet, pyroxene, marble, and hornfels (Figure 4B). The prograde stage is zoned, and the zoning pattern is thick hornfels with parts of pyroxene-bearing pale-brown garnet, banded skarn, marbleization-limestone from the deep to shallow (Figures 3, 4A). The retrograde skarn-sulfide stage is the main mineralization stage. This stage is associated with the formation of steep-dipping branching veins or veinlets and layer-parallel massive ores with dominated ore minerals such as massive pyrrhotite, sphalerite with parts of epidote, cassiterite, arsenian pyrite, and minor chalcopyrite. The euhedral coarse cassiterite ($100\text{--}700 \mu\text{m}$) is followed by pyrrhotite, and then sphalerite base metal sulfides in this stage (Figures 5C,D). The pyrrhotite laths and lamellae, and chalcopyrite blebs intergrew with sphalerite (Figure 5E). The quartz sulfide veins stage is associated with the formation of middle- and steep-dipping veins with the mineral assemblage of arsenopyrite, pyrite, quartz, sericite, and small amounts of chlorite. This stage could be divided into two sub-stages. Anhydrous pyrite, euhedral coarse

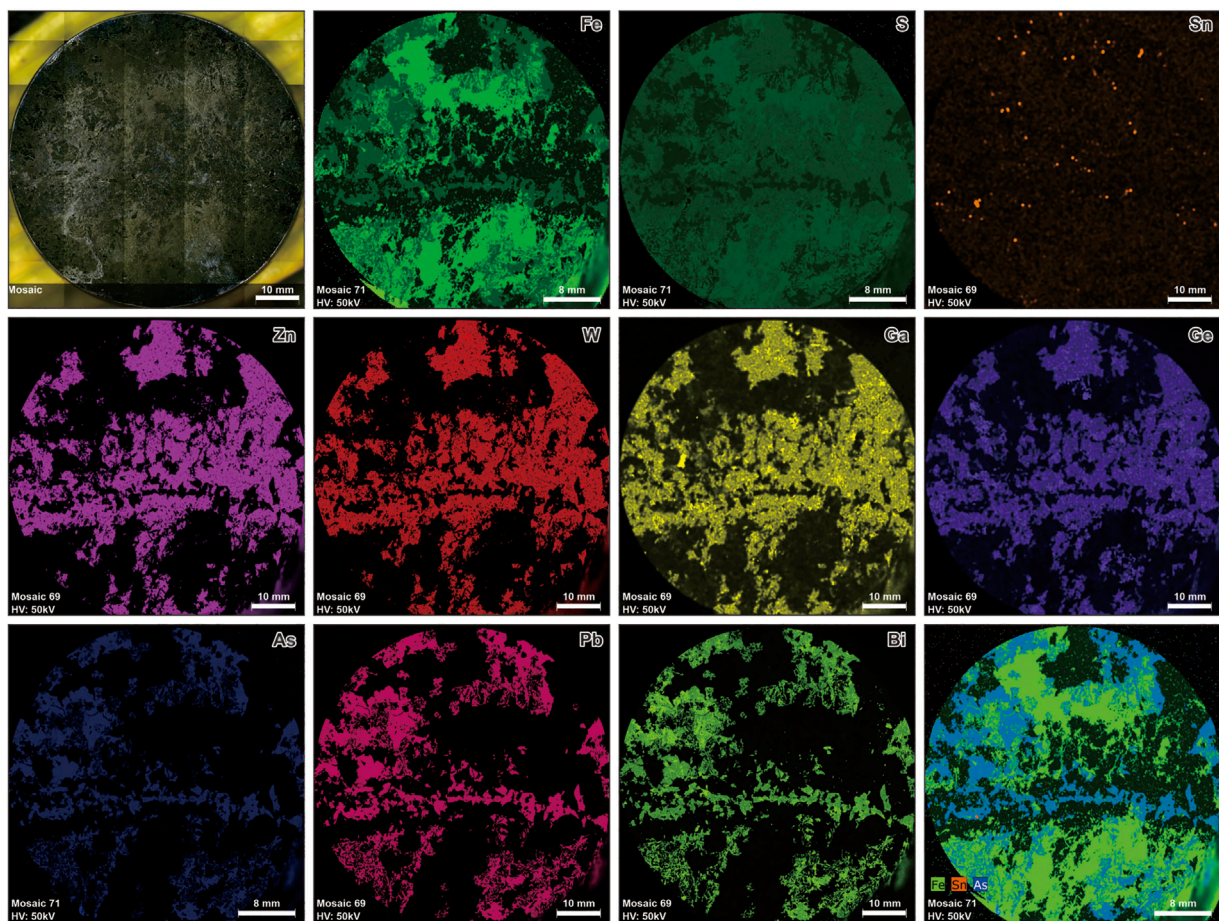


FIGURE 8
Photograph, single-element μ -XRF maps (Fe, S, Sn, Zn, W, Ga, Ge, As, Pb, Bi) and multi-element map of rock slab XLM1902.

arsenopyrite, and fine quartz, sericite of sub-stage I intensively replaced the cassiterite, pyrrhotite, and sphalerite of stage II (Figures 5G,H, 7). The euhedral arsenopyrite-quartz veinlets of sub-stage ii crosscut the veins of sub-stage I (Figure 5F). Steep-dipping barren pyrite-calcite veins (stage IV) crosscut the former veins (Figures 4B,D, 5A,H).

Element mapping

Two polished slabs (XLM1901 and XLM1902) and one thin section (XLM1901T) were measured and elemental distribution maps were obtained. Each map was compared to a reflected light image that came from a section close to the one data was collected from (Figures 6–8).

Figure 6 shows the Fe, S, Si, Sn, Zn, W, Cu, Ga, and Ge distributions compared to the hand specimen of XLM1901. Copper, W, Ga, and Ge show an intensive positive correlation

with Zn. Copper could be proved by chalcopyrite blebs coexisting with sphalerite (Figure 5E). Tungsten mineral is not found in this study. Gallium and Ge are thought to be substituted with Zn in sphalerite. Tin distributed in the top-left corner corresponds to the position of cassiterite. The distribution of Fe with help of S could identify different iron-bearing minerals (pyrrhotite and pyrite) and could determine the paragenetic sequence that pyrite replaced pyrrhotite and sphalerite at the left-bottom of the sample.

Figure 7 shows the Fe, S, Zn, W, Cu, Sn, Al, and Si distributions compared to the hand specimen and reflected light image of XLM1901T. The observed depositional sequences are pyrrhotite + sphalerite + epidote followed by quartz + potassium feldspar + arsenopyrite and pyrite + quartz + calcite veinlet. Some disseminated Sn is distributed in the sphalerite aggregation. The distribution characteristics of other elements are similar to those of the XLM1901.

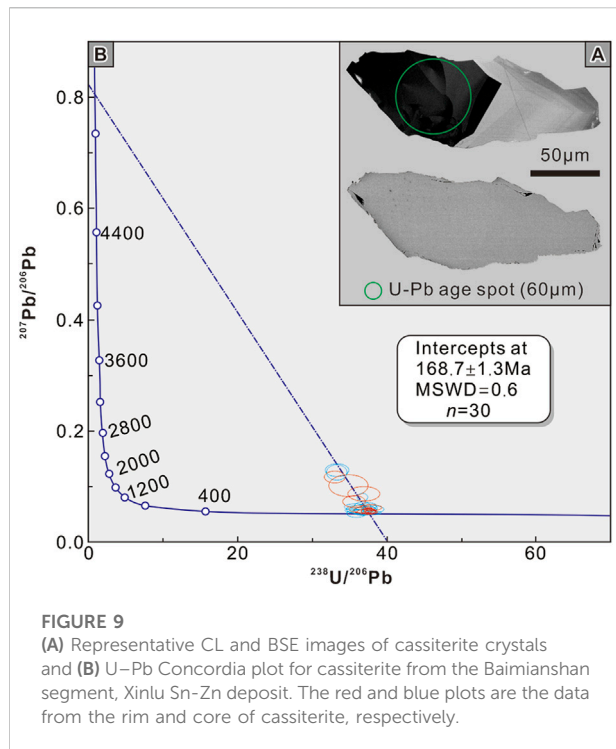


FIGURE 9
(A) Representative CL and BSE images of cassiterite crystals and **(B)** U–Pb Concordia plot for cassiterite from the Baimianshan segment, Xinlu Sn–Zn deposit. The red and blue plots are the data from the rim and core of cassiterite, respectively.

Figure 8 shows single-element distributions of 9 elements (Fe, S, Sn, Zn, W, Pb, Bi, Ga, and Ge), a multi-element map with Fe, Sn, and As, and phases based on multi-element Fe–Zn–As compared to the hand specimen and reflected light image of XLM1902. The distribution characteristics of most elements (Fe, S, Sn, Zn, W, Ga, and Ge) are similar to those of the XLM1901 and XLM1901T. This sample has obvious high counts of As, Pb, and Bi. The high content of As corresponds to the position of arsenopyrite on the reflected light image (Figure 5A), whereas no lead and bismuth minerals were found in this sample. Multi-element maps with Fe, Sn, and As, and phases based on multi-element Fe–Zn–As also clearly reveal the paragenetic sequences of stages II and III.

Cassiterite U–Pb ages

The cassiterite grains are dark brown to black, generally euhedral to subhedral with a size of 100–700 μm . Internal textures of cassiterite are solid dark cores with oscillatory rims. Some cassiterite grains have cracks and are porous with tiny metallic inclusions as revealed by the CL and BSE images (Figure 9A).

The analytical results of U–Pb isotopes of the cassiterite grains are listed in Table 1 and illustrated in Figure 9B. These grains have relatively low total Pb contents of <0.1 ppm, low Th contents of <0.01 ppm, and U contents varying from 0.31 to

2.85 ppm. The analyzed dark cores have higher U concentrations (1.01–2.85 ppm, 1.77 ppm average) than the oscillatory rims (0.31–1.63 ppm, 0.82 ppm average). The plots of 17 cores and 13 rims define a good Concordia line with a lower intercept at 168.7 ± 1.3 Ma (1σ ; MSWD = 0.6; $n = 30$) (Figure 9B).

Discussion

Application of thin section reflection and element mapping

Our results demonstrate the reflection mapping and μ -XRF element mapping on thin section and hand specimens together with detailed petrographic paragenesis in ore deposits can guide the selection of analytical spots for cassiterite U–Pb dating, which would enhance the study of ore formation processes.

Reflection and element mapping of representative samples could provide compositional and mineralogical information across a range of scales. This work is summarized as follows. First, the element mapping could easily distinguish different iron-bearing or sulfur-bearing minerals [such as pyrrhotite (Fe: 63.53%, S: 36.47%), pyrite (Fe: 46.55%, S: 53.45%), arsenopyrite (Fe: 34.3%, S: 19.69%), and sphalerite (Fe: <10%, S: 32.9%)] owing to the differences in theoretical composition. The color intensity of Fe-mineral gradually decreases from pyrrhotite, pyrite, arsenopyrite, and sphalerite (Figures 6–8). At the bottom of Figure 6, the light green parts overlap and crosscut the bright green parts, suggesting that the pyrite was formed later than pyrrhotite. In Figure 8, it is obvious that the light green areas overlap and crosscut the bright green and black areas. This is consistent with the microscopic observation that arsenopyrite replaced pyrrhotite and sphalerite. The color intensity of S gradually decreases from pyrite, pyrrhotite, sphalerite, and arsenopyrite (Figures 6–8). The distribution of Fe and S elements can accurately determine the sequence of mineral formation in the Xinlu deposit. Second, element mapping could provide some information on mineralization that cannot be observed under a microscope. The multi-elements distribution shows that W is positively related to Zn (Figure 8). However, no tungsten mineral (such as sanmartinite) was recognized, implying that the ore-forming fluid was rich in tungsten as supported by the quartz vein type tungsten mineralization after the skarn mineralization in the Xinlu deposit (Gu et al., 2007a; Li S. Z. et al., 2012). In the quartz sulfide veins stage, As, Pb, and Bi show a positive correlation and correspond to the position of arsenopyrite (Figures 6–8). Bismuth-lead sulfosalts may be a reasonable explanation. Bismuth-lead sulfosalt is common in the late stage of tin deposits and well documented in the Sn-sulfide-sulfosalts deposits of the Bolivia Sn province

TABLE 1 LA-ICP-MS U-Pb dating results of cassiterite from the Baimianshan segment, Xinlu Sn-Zn deposit, South China.

Analysis spots		U-Th-Pb contents			U-Pb isotopic ratios					
		²³⁸ U	²³² Th	Common Pb	²⁰⁷ Pb/ ²⁰⁶ Pb	1σ	²⁰⁷ Pb/ ²³⁵ U	1σ	²⁰⁶ Pb/ ²³⁸ U	1σ
XLM from the Baimianshan segment, Xinlu Sn-Zn deposit, South China										
Core	XLM01	1.86	0.00	0.01	0.05703	0.00353	0.21094	0.01273	0.02713	0.00070
	XLM02	1.01	0.00	0.04	0.11751	0.00687	0.48280	0.02807	0.03032	0.00084
	XLM03	1.40	0.00	0.05	0.06371	0.00387	0.24246	0.01479	0.02792	0.00079
	XLM04	1.02	0.00	0.01	0.05935	0.00420	0.22082	0.01569	0.02742	0.00078
	XLM09	2.85	0.00	0.04	0.05236	0.00251	0.18823	0.00890	0.02640	0.00068
	XLM10	2.10	0.00	0.00	0.06203	0.00309	0.22339	0.01127	0.02639	0.00068
	XLM11	1.91	0.00	0.02	0.05784	0.00413	0.20748	0.01435	0.02692	0.00075
	XLM12	1.99	0.00	0.05	0.05423	0.00319	0.19918	0.01220	0.02711	0.00081
	XLM13	1.27	0.00	0.00	0.05670	0.00317	0.20845	0.01188	0.02762	0.00095
	XLM14	1.82	0.00	0.03	0.05473	0.00289	0.19620	0.00997	0.02676	0.00068
	XLM17	1.63	0.00	0.04	0.06507	0.00371	0.23344	0.01210	0.02664	0.00052
	XLM18	1.29	0.00	0.00	0.06184	0.00389	0.22389	0.01404	0.02648	0.00046
	XLM19	1.95	0.00	0.01	0.05530	0.00301	0.20043	0.01061	0.02666	0.00046
	XLM20	2.53	0.00	0.02	0.05379	0.00213	0.19805	0.00855	0.02651	0.00042
	XLM24	1.51	0.00	0.01	0.05982	0.00344	0.21782	0.01228	0.02663	0.00042
	XLM25	1.98	0.00	0.03	0.05588	0.00289	0.20491	0.01034	0.02687	0.00033
	XLM27	1.93	0.00	0.02	0.05662	0.00256	0.20861	0.00968	0.02669	0.00033
Rim	XLM05	0.44	0.00	0.01	0.10130	0.01294	0.44026	0.07709	0.02870	0.00143
	XLM06	0.47	0.00	0.03	0.07352	0.00702	0.26956	0.02122	0.02808	0.00080
	XLM07	0.31	0.00	0.02	0.08698	0.00885	0.30960	0.02723	0.02709	0.00103
	XLM08	0.73	0.00	0.00	0.12933	0.00790	0.53831	0.03588	0.03006	0.00095
	XLM15	0.55	0.00	0.05	0.05872	0.00509	0.21787	0.01968	0.02696	0.00122
	XLM16	0.55	0.00	0.02	0.12528	0.00910	0.49936	0.03468	0.03006	0.00084
	XLM21	1.63	0.00	0.02	0.05570	0.00330	0.20408	0.01195	0.02658	0.00047
	XLM22	0.51	0.00	0.00	0.05217	0.00494	0.19877	0.01906	0.02784	0.00070
	XLM23	0.69	0.00	0.00	0.05504	0.00477	0.20303	0.01608	0.02724	0.00062
	XLM26	1.93	0.00	0.04	0.05438	0.00248	0.19697	0.00927	0.02639	0.00039
	XLM28	0.58	0.00	0.02	0.06435	0.00521	0.23583	0.01727	0.02725	0.00054
	XLM29	1.01	0.00	0.02	0.08087	0.00476	0.30205	0.01766	0.02723	0.00037
	XLM30	1.23	0.00	0.05	0.05619	0.00305	0.20395	0.01132	0.02648	0.00035
Standard cassiterite AY-4										
	AY-4std	1.46	0.00	0.3	0.52392	0.01993	5.07543	0.37015	0.06793	0.00364
	AY-4std	6.09	0.03	0.8	0.43967	0.02259	3.86378	0.41684	0.05767	0.00423
	AY-4std	0.92	0.00	0.1	0.49297	0.04751	3.92224	0.38889	0.05402	0.00284
	AY-4std	345	0.00	41	0.31090	0.03718	3.34334	0.66889	0.05364	0.00670
	AY-4std	1.45	0.00	0.1	0.27295	0.01958	1.54498	0.15290	0.03628	0.00151
	AY-4std	147	0.00	4.3	0.21764	0.01115	0.98451	0.06717	0.03179	0.00074
	AY-4std	1.92	0.00	0.1	0.20174	0.01508	0.95790	0.09040	0.03142	0.00094
	AY-4std	3.21	0.00	0.2	0.19384	0.01778	0.89486	0.07745	0.03020	0.00120
	AY-4std	67	0.00	1.7	0.16370	0.01996	0.66193	0.07045	0.02790	0.00087
	AY-4std	8.65	0.00	0.4	0.14081	0.01539	0.62852	0.07514	0.02765	0.00096

(Continued on following page)

TABLE 1 (Continued) LA-ICP-MS U-Pb dating results of cassiterite from the Baimianshan segment, Xinlu Sn-Zn deposit, South China.

Analysis spots	U-Th-Pb contents			U-Pb isotopic ratios					
	²³⁸ U	²³² Th	Common Pb	²⁰⁷ Pb/ ²⁰⁶ Pb	1σ	²⁰⁷ Pb/ ²³⁵ U	1σ	²⁰⁶ Pb/ ²³⁸ U	1σ
AY-4std	3.14	0.00	0.0	0.11874	0.01239	0.46164	0.04956	0.02719	0.00104
AY-4std	0.08	0.00	0.0	0.10436	0.02845	0.30422	0.07150	0.02689	0.00149
AY-4std	15	0.00	0.0	0.08293	0.00559	0.31168	0.02182	0.02677	0.00071
AY-4std	66	0.00	1.7	0.12044	0.01668	0.46544	0.05747	0.02637	0.00092
AY-4std	0.97	0.00	0.0	0.08996	0.00466	0.32390	0.01752	0.02615	0.00040
AY-4std	213	0.00	3.9	0.12359	0.01338	0.45961	0.04720	0.02611	0.00072
AY-4std	49	0.00	0.5	0.06693	0.00801	0.23368	0.02575	0.02497	0.00077
AY-4std	14	0.00	1.0	0.07360	0.01043	0.21904	0.02460	0.02300	0.00071
NIST reference glass SRM 612									
SRM 612	98	37		0.92112	0.12499	32.90046	3.71038	0.24484	0.00826
SRM 612	101	39		0.92721	0.11829	33.63997	3.56754	0.24918	0.00790
SRM 612	100	38		0.94022	0.07948	34.05289	2.52080	0.25511	0.00470
SRM 612	100	38		0.94842	0.08621	34.95647	2.77951	0.25968	0.00513
SRM 612	99	37		0.84393	0.04970	27.21569	1.65231	0.22700	0.00365
SRM 612	100	38		0.83753	0.04991	26.80127	1.64293	0.22487	0.00360
SRM 612	37	37		0.93942	0.07635	29.77904	2.28620	0.22463	0.00840
SRM 612	38	39		0.94003	0.07406	29.79229	2.22115	0.22455	0.00813
SRM 612	37	37		0.91044	0.02008	28.89959	0.72585	0.22739	0.00214
SRM 612	38	38		0.90875	0.02065	28.97643	0.74343	0.22848	0.00216
SRM 612	38	39		0.92143	0.01898	28.86141	0.71193	0.22596	0.00157
SRM 612	36	36		0.92808	0.01973	29.00782	0.72734	0.22568	0.00184

(Gemmrich et al., 2021; Routhier, 1980), the Dachang Sn-Zn district (Huang et al., 1986; Fan et al., 2004), and the Bawang Fe-Zn-Sn deposit of Wuxu Sb-Zn district, South China (Xiao et al., 2022). Based on the two above-mentioned works, the generated elemental maps can provide information on the mineralization process and more meaningful results than a single micro-observation.

Reflection and element mapping can also greatly improve the efficiency of positioning for cassiterite U-Pb dating when the sample contains minor cassiterite. Commonly, it is hard to identify the position of cassiterite in the coexistence of fine-grained cassiterite and sphalerite sulfide. In our study, the element mapping by μ -XRF all display the distribution of tin (Figures 6–8), which was then confirmed to be cassiterite by quick microscopic observation (Figures 5C,D). Therefore, we confirm that the cassiterite was only formed in the retrograde skarn-sulfide stage. Moreover, the element mapping also avoided potential mixed ages of cassiterite. This method is also a powerful tool for *in situ* geochronology of polyphase minerals and provides a more accurate process of mineralization.

Age relationship between Sn-Zn (-W) mineralization and magmatism of Guposhan-Huashan district during Jurassic

Published high-precision geochronological investigations, including zircon U-Pb and biotite ⁴⁰Ar-³⁹Ar dating on the causative intrusions and multiple dating methods (Sm-Nd, Re-Os, ⁴⁰Ar-³⁹Ar, Rb-Sr) on the skarn and hydrothermal minerals, have revealed the magma emplacement and mineralization in the Guposhan-Huashan district. However, the relationship between the Sn-Zn (-W) mineralization and magmatism remains confusing based on these studies. An overview of the timing of magmatic-hydrothermal ore formation in the Guposhan-Huashan district is described as follows.

The Huashan and Guposhan complex plutons are the main intrusions in this district. The Huashan complex pluton composes of Huashan biotite granite in the core, the Tong'an quartz monzonite in the west, and the Niuniao diorite in the southeast. Available zircon U-Pb ages show these three intrusions

were formed at 160–163 Ma (Zhao et al., 2010). The $\epsilon_{\text{Hf}}(t)$ (−2.8 to +7.4), $\epsilon_{\text{Nd}}(t)$ (−3.18 to +0.91), and initial ($^{87}\text{Sr}/^{86}\text{Sr}$) ratios (0.70472–0.70714) revealed these three intrusions were generated by mantle-crust interaction (Cai et al., 2018 and references therein; Zhao et al., 2010; Zhu et al., 2005, 2006). Zhu et al. (2006) reported the younger felsic dykes with an age of 148.0 ± 4.0 Ma intruded into the Huashan granite along the fractures. The Guposhan complex pluton includes Lisong hornblende biotite granite in the core, Guposhan coarse biotite granite, and Fengmichong fine felsic dykes in the south (Figure 2A). Published zircon U-Pb ages show that the Lisong and Guposhan granites were formed at 161.0–163.0 Ma and 159.5–165.0 Ma, respectively (Zhu et al., 2006; Gu et al., 2007b; Zhao et al., 2010; Shu et al., 2011; Cai et al., 2020; Cao et al., 2020). Li et al. (2016) dated the causative Shimen quartz monzodiorite in the Xinlu deposit and Fengmichong biotite granite in the Shuiyanba deposit by igneous biotites ^{40}Ar - ^{39}Ar dating at 168.7 ± 1.9 Ma and 165.0 ± 1.1 Ma, respectively. The $\epsilon_{\text{Hf}}(t)$ (−3.6 to −2.3), $\epsilon_{\text{Nd}}(t)$ (−5.5 to +1.9), and initial ($^{87}\text{Sr}/^{86}\text{Sr}$) ratios (0.70473–0.70742) of the Lisong and Guposhan granites and dark mafic enclaves imply the Guposhan main pluton also resulted from mantle-crust interaction. The later felsic dykes were dated by zircon U-Pb at 146.8 ± 2.3 Ma to 154.2 ± 3.1 Ma (Zhu et al., 2006; Wang et al., 2014). Initial Sr isotopic data ($(^{87}\text{Sr}/^{86}\text{Sr})_i = 0.7173$) and $\epsilon_{\text{Nd}}(t)$ (−5) of later felsic dykes are obvious different from those of the main pluton in this district (Gu et al., 2007b). The high initial Sr isotopic and low $\epsilon_{\text{Nd}}(t)$ values suggest the later dykes were generated from crust components. Thus, based on geochronology, two episodes of magmatism (159.5–168.7 Ma and 146.8–154.2 Ma) occurred in the Guposhan-Huashan district during Jurassic, of which the former was predominant.

Our robust *in-situ* LA-ICP-MS cassiterite U-Pb data, integrated with previous geochronological studies, support one stage magmatic-hydrothermal mineralization associated with 159.5–168.7 Ma magmatism in this district. Our new age directly yielded from cassiterite in this study demonstrates that the Sn-Zn mineralization in the Baimianshan segment occurred at 168.7 ± 1.3 Ma, coinciding with the age of quartz monzodiorite in the Xinlu deposit. Cassiterite U-Pb age is a little older than muscovite ^{40}Ar - ^{39}Ar age of skarn-type ores (160.0 ± 2.0 Ma) and molybdenite Re-Os age of quartz-vein type wolframite ores (154.4 ± 3.5 Ma) from the Liuheo segment (Feng et al., 2019). Due to the lack of detailed microscopic observation, the muscovite ^{40}Ar - ^{39}Ar isotopic data are doubtful to represent the skarn stage. Li et al. (2016) obtained hydrothermal muscovite ^{40}Ar - ^{39}Ar age of 160.6 ± 1.5 Ma for the Liuheo altered granite. Therefore, we could speculate the muscovite ^{40}Ar - ^{39}Ar isotopic data obtained by Feng et al. (2019) may represent the age of the quartz-vein stage rather than the skarn stage. This conclusion could be supported by the euhedral sericite-quartz of stage III replacing the massive skarn-type pyrrhotite and sphalerite of stage II (Figures 5A,H). From a temporal perspective, the skarn Sn-Zn mineralization is associated with quartz monzodiorite.

Spatially, the skarn Sn-Zn mineralization is related to the Guposhan coarse biotite granite.

In the following, we also compare the obtained cassiterite U-Pb age to published geochronological data of mineralization in the Guposhan-Huashan district to further constrain the Sn-Zn-W formation age. Previous work on the mineralization age of the Shuiyanba Sn deposit used muscovite ^{40}Ar - ^{39}Ar dating (162.0 ± 1.9 Ma and 162.5 ± 1.2 Ma; Kang et al., 2012; Li et al., 2016) of quartz + muscovite + wolframite veins and Rb-Sr dating of quartz fluid inclusions (136.1 ± 2.0 Ma; Gu et al., 2007a) from the wolframite + scheelite + arsenopyrite + cassiterite quartz veins in the Lantoushan segment. It is difficult to confirm whether the Rb-Sr isotopes of different hand specimens were at isotopic equilibrium or the ore-forming fluids have homogeneous initial $^{87}\text{Sr}/^{86}\text{Sr}$ ratios. Furthermore, quartz from the W-Sn quartz veins has a different initial $^{87}\text{Sr}/^{86}\text{Sr}$ ratio (0.72015–0.72735) from the Guposhan-Huashan pluton (0.7056–0.7066) (Gu et al., 2007b). To sum up, the muscovite ^{40}Ar - ^{39}Ar dating results are more reliable and the quartz vein type W-Sn mineralization of the Shuiyanba Sn deposit probably occurred at 162 Ma.

Published Sm-Nd isotopic data of skarn minerals (pyroxene, hornblende, garnet) from the skarn-type ores in the Chuanlingjiao segment of the Keda Sn deposit suggest the skarn minerals occurred at 160.4 ± 4.8 Ma (Cao et al., 2020). Li et al. (2016) obtained muscovite ^{40}Ar - ^{39}Ar ages of 164.5 ± 2.6 Ma for W-Sn quartz veins hosted in the Devonian marble at Maohedong segment and 161.2 ± 1.3 Ma for wolframite bearing quartz veins hosted in the Devonian sandstone at Sanchachong segment. According to the above, both the skarn Sn and quartz vein W-Sn mineralization occurred during 160–164 Ma.

As aforementioned, we conclude the Sn-W mineralization in the Guposhan-Huashan district was related to the intermediate felsic intrusions rather than the later felsic dykes. The skarn mineral Sm-Nd isotopic data represent the formation age of the prograde skarn stage (Stage I). Our new cassiterite U-Pb age represents the formation age of retrograde massive skarn-sulfides (stage II). All the muscovite ^{40}Ar - ^{39}Ar ages represent the formation ages of quartz sulfide veins (stage III). No geochronological data of barren carbonate stage (stage IV) have been obtained in the Guposhan-Huashan district to date.

Relationship between the subduction of Paleo-Pacific plate and Jurassic tin-tungsten mineralization in the Nanling belt of South China

To understand the timing of magmatic-hydrothermal ore formation on the scale of the Nanling belt and SCB, we incorporated our new geochronological data into the existing

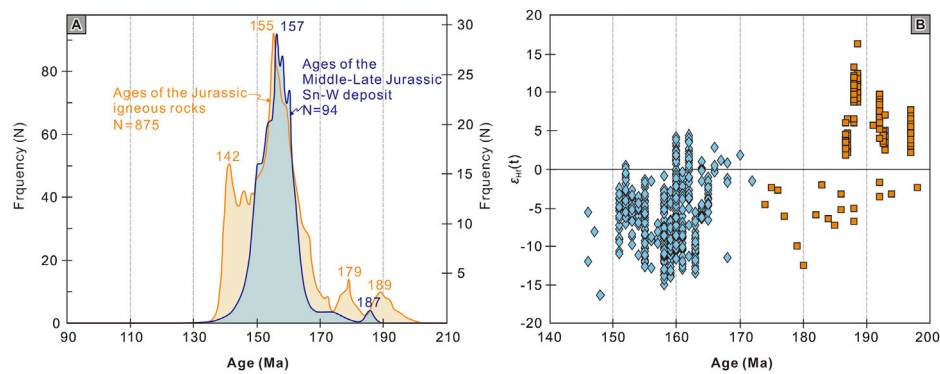


FIGURE 10

(A) Histogram of the Jurassic igneous rocks and Sn-W mineralization in South China. Data are from Cao et al., 2021; Feng et al., 2019; Mao et al., 2019; Xiao et al., 2019, and references therein. (B) $\epsilon_{\text{Hf}}(t)$ -age diagram for zircons from the Jurassic igneous rocks, South China. Data are from Li et al., 2018, Yang et al., 2021, and references therein. The orange square represents the Early Jurassic igneous rocks with ages of 174–198 Ma. The slightly blue rhombus represents the Middle-Late Jurassic igneous rocks with ages of 146–172 Ma.

geochronological framework of the Nanling Sn-W belt and South China W-Sn provinces during the Jurassic. On the probability density distribution plots of the Jurassic intrusions, two main peaks (~142 and 155 Ma) and two small peaks (~179 and 189 Ma) can be recognized (Figure 10A). The former two peaks with dominated negative $\epsilon_{\text{Hf}}(t)$ values were associated with W-Sn mineralization, whereas the latter two peaks with dominated positive $\epsilon_{\text{Hf}}(t)$ values were associated with Mo-Co mineralization (Figure 10B; Li et al., 2018; Yang et al., 2021). The four age clusters indicate multiphase tectonic events in the SCB. On the probability density distribution plots of the Jurassic W-Sn mineralization, a single peak (~157 Ma) is observed. The W-Sn formation ages overlapped with the second peak of intrusions (Figure 10A). The spatial distribution of W-Sn mineralization and associated intrusions display a slight southeastward younging trend in the Nanling Belt. However, in the entire South China, this trend is not obvious (Figure 1C). Recent research shows that W-Sn mineralization causative intrusions are A-type granites (Li et al., 2018; Xiao et al., 2019; Mao et al., 2021b). It is commonly accepted that the Jurassic mafic-ultramafic intrusions, A-type granites, and bimodal basalt-rhyolite volcanic rocks are formed in the extensional setting, but the geodynamic setting is still puzzling (Zhou and Li, 2000; Zhou et al., 2006; Li and Li, 2007; He et al., 2010; Mao et al., 2021b; Cao et al., 2021). The generally accepted dynamic domain includes the Paleo-Tethyan domain to the southwest and the Paleo-Pacific domain to the southeast. Therefore, two models have been proposed for the Jurassic evolution, including the Paleo-Tethyan post-collisional intra-continental extension model (He et al., 2010; Gan et al., 2017) and Izanagi or Paleo-Pacific plate subduction-related model (Zhou et al.,

2006; Li and Li, 2007; Zaw et al., 2007; Mao et al., 2021b; Cao et al., 2021; Gan et al., 2021). Although the latter view is more popular, it is inconsistent with the fact that the orientation of the distribution of Middle-Late Jurassic rocks is opposite to the subduction of the Paleo-Pacific plate (Gan et al., 2017). The difference in geochemical signatures between the Early-Middle Jurassic mafic and shoshonitic rocks and Cretaceous arc-related rocks in the SCB also indicate that the Paleo-Pacific slab-derived components didn't modify the lithospheric mantle (Gan et al., 2021 and references therein). This conclusion is also confirmed by previous whole rock geochemistry and Sr-Nd-Hf isotope and zircon Hf-O isotope data from the early Jurassic gabbro-syenite-alkali-feldspar granite in South China (Yang et al., 2021). As described above, many facts are still in debate in the Paleo-Pacific subduction model, such as the variations of slab dip angles (Zhou et al., 2006; Li et al., 2018); flat-slab subduction and slab foundering (Li and Li, 2007); polyphase slab subduction and retreat (Li et al., 2020); slab window in the back-arc region (Mao et al., 2021b); and mantle upwelling model (Cao et al., 2021). According to the available data, the Paleo-Pacific subduction model is currently the most reasonable one. First, the geochemical signatures and higher zircon $\epsilon_{\text{Hf}(t)}$ - $\delta^{18}\text{O}$ values of the Middle-Late Jurassic igneous rocks all indicate an extensional setting corresponding to asthenospheric upwelling and crust-mantle interaction (Cao et al., 2021; Gan et al., 2021 and references therein). Previous studies have shown that tin granites generally occurred in an extensional environment corresponding to mantle upwelling (Romer and Kroner, 2016; Xiao et al., 2019; Guo et al., 2021). The upwelling of the basaltic intrusions might provide additional heat and trigger a partial melting of the lower crust to form W-Sn causative granite. Second, the Jurassic compressional deformation in the SCB is consistent with the

coeval advancing motion of the Izanagi trench (Li X. F. et al., 2012; Cao et al., 2021). The Jurassic arc-related granitoids have been also observed in the coastal regions and the South China Sea basin (Xu et al., 2017). Cao et al. (2021) also pointed out that Jurassic magmatism was accompanied by crustal deformation in the SCB. Last, numerical models suggest that flat-slab exists (Dai et al., 2020).

Conclusion

- (1) Thin section reflection and μ -XRF element mapping represent a powerful tool for determining paragenesis in ore deposits and are highly effective to guide the selection of analytical points for cassiterite U-Pb dating. This method may also be applicable for *in-situ* dating of other minerals.
- (2) Four mineralization episodes are identified in the Baimianshan segment, Xinlu deposit. They are prograde skarn (stage I), retrograde skarn-sulfide (stage II), quartz sulfide veins (stage III), and barren carbonate (stage IV) stages. The retrograde skarn-sulfide stage is the main mineralization stage and consists of massive pyrrhotite, and sphalerite with parts of epidote, cassiterite, and minor chalcocopyrite and arsenian pyrite.
- (3) The time of retrograde skarn-sulfide mineralization is dated by LA-ICP-MS cassiterite U-Pb at 168.7 ± 1.3 Ma. Our robust *in-situ* LA-ICP-MS cassiterite U-Pb data, coupled with previous geochronological studies, support one stage magmatic-hydrothermal mineralization associated with 159.5–168.7 Ma magmatism in the Guposhan-Huashan district.
- (4) The Xinlu Sn-Zn mineralization and the Middle-Late Jurassic Sn-W mineralization in the Nanling belt, South China corresponded to asthenospheric upwelling and crust-mantle interaction caused by the subduction of the Paleo-Pacific plate.

Data availability statement

The original contributions presented in the study are included in the article/supplementary material, further inquiries can be directed to the corresponding author.

References

- Cai, Y. F., Liu, F. L., Feng, Z. H., Zhou, Y., and Zeng, C. Y. (2020). Mineral compositional and chronological characteristics of Guposhan pluton in Guangxi and its petrogenetic and metallogenic significance. *J. Jilin Univ. Earth Sci. Ed.* 50 (03), 842–856. doi:10.13278/j.cnki.jjuese.20180316
- Cai, Y. F., Ma, Y. C., Zhou, Y., Su, X. Q., Feng, Z. H., Ma, L. H., et al. (2018). Characteristics of mineralogy, geochronology and geochemistry of the granite in Huashan, Guangxi and its tectonic implication. *Geol. Explor.* 54 (05), 940–956. (in Chinese with English abstract). doi:10.13712/j.cnki.dzykt.2018.05.006
- Cao, J. Y., Yang, X. Y., Lu, Y., Fu, J. M., and Yang, L. Z. (2020). Zircon U-Pb and Sm-Nd geochronology and geochemistry of the Sn-W deposits in the northern

Author contributions

C-HX designed the study, collected the samples for analysis, and compiled the results and wrote the manuscript. P-PY and X-HL collected and processed previously published data. X-HL also finished the figures and table. C-HX and W-LW performed the μ -XRF analysis and process of the data. Y-WT performed cassiterite U-Pb dating and process of the data. X-CL, P-PY, YZ provided feedback to the manuscript.

Funding

This research was jointly supported by the National Natural Science Foundation of China (Grants: 41702095), the CGS Research Fund (Grants: DZLXJK202203) and the China Geological Survey (Grants: DD20190161, DD20221600-3).

Acknowledgments

We would like to thank Xing-Wen Le and Changshan Wei for his help in the field works. We also thank Guest Editor Fan Yang for his handling our paper, and Hua-Wen Cao and other three reviewers for their constructive comments that greatly improved our paper.

Conflict of interest

The authors declare that the research was conducted in the absence of any commercial or financial relationships that could be construed as a potential conflict of interest.

Publisher's note

All claims expressed in this article are solely those of the authors and do not necessarily represent those of their affiliated organizations, or those of the publisher, the editors and the reviewers. Any product that may be evaluated in this article, or claim that may be made by its manufacturer, is not guaranteed or endorsed by the publisher.

Guposhan ore field, Nanling Range, southern China. *Ore Geol. Rev.* 118, 103323. doi:10.1016/j.oregeorev.2020.103323

Cao, X. Z., Flament, N., Li, S. Z., and Müller, R. D. (2021). Spatio-temporal evolution and dynamic origin of Jurassic-Cretaceous magmatism in the South China Block. *Earth. Sci. Rev.* 217, 103605. doi:10.1016/j.earscirev.2021.103605

Cawood, P. A., Zhao, G. C., Yao, J. L., Wang, W., Xu, Y. J., and Wang, Y. J. (2018). Reconstructing south China in phanerozoic and precambrian supercontinents. *Earth. Sci. Rev.* 186, 173–194. doi:10.1016/j.earscirev.2017.06.001

- Dai, L., Wang, L., Lou, D., Li, Z. H., Dong, H., Ma, F., et al. (2020). Slab rollback versus delamination: Contrasting fates of flat-slab subduction and implications for south China evolution in the mesozoic. *J. Geophys. Res. Solid Earth* 125 (4). doi:10.1029/2019JB019164
- Dong, Z. C. (1991). The REE Geochemical characteristics in the Xinlu tin orefield, Guangxi. *J. Guilin Inst. Technol.* 011 (003), 277–286.
- Fan, D., Zhang, T., Ye, J., Pašava, J., Kribek, B., Dobes, P., et al. (2004). Geochemistry and origin of tin–polymetallic sulfide deposits hosted by the Devonian black shale series near Dachang, Guangxi, China. *Ore Geol. Rev.* 24 (1–2), 103–120. doi:10.1016/j.oregeorev.2003.08.006
- Feng, Y., Feng, Z. H., Fu, W., Kang, Z. Q., Jiang, J., Guo, A., et al. (2019). Magmatic-hydrothermal mineralization sequence in Xinlu ore field, Guangxi, south China: Constraints from zircon U–Pb, molybdenite Re–Os, and muscovite Ar–Ar dating. *Resour. Geol.* 69 (4), 430–447. doi:10.1111/rge.12212
- Flude, S., Haschke, M., and Storey, M. (2017). Application of benchtop micro-XRF to geological materials. *Mineral. Mag.* 81 (4), 923–948. doi:10.1180/minmag.2016.080.150
- Gan, C. S., Wang, Y. J., Zhang, Y. Z., and Zhang, J. (2017). The earliest Jurassic A-type granite in the Nanling Range of southeastern South China: Petrogenesis and geological implications. *Int. Geol. Rev.* 59 (3), 274–292. doi:10.1080/00206814.2016.1254574
- Gan, C., Zhang, Y. Z., Wang, Y. J., Qian, X., and Wang, Y. (2021). Reappraisal of the mesozoic tectonic transition from the paleo-tethyan to paleo-pacific domains in south China. *GSA Bull.* 133 (11–12), 2582–2590. doi:10.1130/B35755.1
- Gemmrich, L., Torró, L., Melgarejo, J. C., Laurent, O., Vallance, J., Chelle-Michou, C., et al. (2021). Trace element composition and U–Pb ages of cassiterite from the Bolivian tin belt. *Min. Deposita* 56, 1491–1520. doi:10.1007/s00126-020-01030-3
- Gilder, S. A., Gill, J., Coe, R. S., Zhao, X., Liu, Z., Wang, G., et al. (1996). Isotopic and paleomagnetic constraints on the Mesozoic tectonic evolution of south China. *J. Geophys. Res.* 101 (B7), 16137–16154. doi:10.1029/96JB00662
- Gu, S. Y., Hua, R. M., and Qi, H. W. (2007a). A genetic study of Xinlu-Shuiyanba W–Sn orefield, Northeast Guangxi. *Min. Depos.* 3, 265–276. (in Chinese with English abstract). doi:10.16111/j.0258-7106.2007.03.003
- Gu, S. Y., Hua, R. M., and Qi, H. W. (2007b). Zircon LA-ICP-MS U–Pb dating and Sr–Nd isotope study of the Guposhan granite complex, Guangxi, China. *Chin. J. Geochem.* 26 (03), 290–300. doi:10.1007/s11631-007-0290-5
- Guo, J., Wu, K., Seltmann, R., Zhang, R., Ling, M., Li, C., et al. (2021). Unraveling the link between mantle upwelling and formation of Sn-bearing granitic rocks in the world-class Dachang tin district, South China. *GSA Bull.* 134 (3–4), 1043–1064. doi:10.1130/B35492.1
- He, Z. Y., Xu, X. S., and Niu, Y. (2010). Petrogenesis and tectonic significance of a Mesozoic granite-syenite-gabbro association from inland South China. *Lithos* 119 (3–4), 621–641. doi:10.1016/j.lithos.2010.08.016
- Hu, H. Y., Qiu, L. B., Xie, G. Y., and You, J. S. (1992). Metallogenic regularities and prediction of concealed deposits in the Xinlu tin orefield Guangxi, China. *Geotecton. Metallog.* 03, 221–238. (in Chinese with English abstract). doi:10.16539/j.dgzyckx.1992.03.001
- Hu, R. Z., and Zhou, M. F. (2012). Multiple Mesozoic mineralization events in South China – an introduction to the thematic issue. *Min. Depos.* 47, 579–588. doi:10.1007/s00126-012-0431-6
- Huang, M. Z., Wu, G. B., Chen, Y. C., and Tang, S. H. (1986). Mineralogical study of the franckite from the Dachang cassiterite-sulphide polymetallic ore field, Guangxi. *Acta Geol. Sin.* 2, 164–175. (in Chinese with English abstract).
- Kang, Z. Q., Feng, Z. H., Li, X. F., Liao, J. F., Yu, Y., and Pan, H. B. (2012). 40Ar–39Ar age of muscovite in the Shuiyanba tungsten-tin ore field in Northeast Guangxi and its geological significance. *Bull. Mineral. Pet. Geochem.* 31 (6), 606–611. (in Chinese with English abstract). doi:10.3969/j.issn.1007-2802.2012.06.008
- Li, H., Palinkaš, L. A., Watanabe, K., and Xi, X. S. (2018). Petrogenesis of Jurassic A-type granites associated with Cu–Mo and W–Sn deposits in the central Nanling region, South China: Relation to mantle upwelling and intra-continental extension. *Ore Geol. Rev.* 92, 449–462. doi:10.1016/j.oregeorev.2017.11.029
- Li, J. H., Cawood, P. A., Ratschbacher, L., Zhang, Y. Q., Dong, S. W., Xin, Y. J., et al. (2020). Building Southeast China in the late Mesozoic: Insights from alternating episodes of shortening and extension along the Lianhuashan fault zone. *Earth. Sci. Rev.* 201, 103056. doi:10.1016/j.earscirev.2019.103056
- Li, J. H., Zhang, Y. Q., Ratschbacher, L., Zhao, G. C., Dong, S. W., Xin, Y. J., et al. (2022). Polyphase deformation in the badu complex: Insights into triassic intraplate orogeny in south China. *J. Struct. Geol.* 154, 104475. doi:10.1016/j.jsg.2021.104475
- Li, S. Z., Santosh, M., Zhao, G. C., Zhang, G. W., and Jin, C. (2012). Intracontinental deformation in a frontier of super-convergence: A perspective on the tectonic milieu of the south China block. *J. Asian Earth Sci.* 49, 313–329. doi:10.1016/j.jseas.2011.07.026
- Li, X. F., Feng, Z. H., Xiao, R., Song, C. A., Feng, Y., and Wang, C. Y. (2012). Spatial and temporal distributions and the geological setting of the W–Sn–Mo–Nb–Ta deposits at the northeast Guangxi, south China. *Acta Geol. Sin.* 86 (11), 1713–1725. (in Chinese with English abstract). doi:10.3969/j.issn.0001-5717.2012.11.001
- Li, X. F., Xiao, R., Feng, Z. H., Wei, C. X., Tang, Y. W., Bai, Y. P., et al. (2016). Ar–Ar ages of hydrothermal muscovite and igneous biotite at the guposhan-huashan district, northeast Guangxi, south China: Implications for mesozoic W–Sn mineralization. *Resour. Geol.* 65 (2), 160–176. doi:10.1111/rge.12062
- Li, Z. X., and Li, X. H. (2007). formation of the 1300-km-wide intracontinental orogen and postorogenic magmatic province in mesozoic south China: A fl at-slab subduction model. *Geol.* 35 (2), 179–182. doi:10.1130/G23193A.1
- Liu, Y. S., Hu, Z. C., Gao, S., Günther, D., Xu, J., Gao, C. G., et al. (2008). *In situ* analysis of major and trace elements of anhydrous minerals by LA-ICP-MS without applying an internal standard. *Chem. Geol.* 257, 34–43. doi:10.1016/j.chemgeo.2008.08.004
- Ludwig, K. R. (2003). *Isoplot v. 3.0: a geochronological toolkit for microsoft excel*, 4. USA: Berkeley Geochronology Center, 1–70. Special Publication.
- Mao, J. W., Liu, P., Goldfarb, R. J., Goryachev, N. A., Pirajno, F., Zheng, W., et al. (2021a). Cretaceous large-scale metal accumulation triggered by post-subductional large-scale extension, East Asia. *Ore Geol. Rev.* 136, 104270. doi:10.1016/j.oregeorev.2021.104270
- Mao, J. W., Zheng, W., Xie, G. Q., Lehmann, B., and Goldfarb, R. (2021b). Recognition of a Middle-Late Jurassic arc-related porphyry copper belt along the southeast China coast: Geological characteristics and metallogenic implications. *Geology* 49 (5), 592–596. doi:10.1130/G48615.1
- Meinert, L. D., Dipple, G. M., Nicolescu, S., Hedenquist, J. W., Thompson, J. F. H., Goldfarb, R. J., et al. (2005). “World skarn deposits,” in *One hundredth anniversary volume* (USA: Society of Economic Geologists). doi:10.5382/AV100.11
- Ou, Z. Y. (1989). Analysis of structural control on mineralization and metallogenic prognosis in Xinlu tin orefield Guangxi. *J. Guilin Inst. Technol.* 04, 387–397. (in Chinese with English abstract).
- Romer, R. L., and Kroner, U. (2016). Phanerozoic tin and tungsten mineralization–Tectonic controls on the distribution of enriched protoliths and heat sources for crustal melting. *Gondwana Res.* 31, 60–95. doi:10.1016/j.gr.2015.11.002
- Shu, L. S. (2012). An analysis of principal features of tectonic evolution in South China Block. *Geol. Bull. China* 31 (07), 1035–1053. (in Chinese with English abstract). doi:10.3969/j.issn.1671-2552.2012.07.003
- Shu, L. S., Yao, J. L., Wang, B., Faure, M., Charvet, J., and Chen, Y. (2021). Neoproterozoic plate tectonic process and Phanerozoic geodynamic evolution of the South China Block. *Earth. Sci. Rev.* 216, 103596. doi:10.1016/j.earscirev.2021.103596
- Shu, X. J., Wang, X. L., Sun, T., Xu, X., and Dai, M. N. (2011). Trace elements, U–Pb ages and Hf isotopes of zircons from Mesozoic granites in the Western Nanling Range, South China: Implications for petrogenesis and W–Sn mineralization. *Lithos* 127 (3–4), 468–482. doi:10.1016/j.lithos.2011.09.019
- Tang, Y. W., Han, J. J., Lan, T. G., Gao, J. F., Liu, L., Xiao, C. H., et al. (2022). Two reliable calibration methods for accurate *in-situ* U–Pb dating of scheelite. *J. Anal. At. Spectrom.* 37 (2), 358–368. doi:10.1039/D1JA00387A
- Wang, H., Treble, P., Baker, A., Rich, A. M., Bhattacharyya, S., Oriani, F., et al. (2022). Sulphur variations in annually layered stalagmites using benchtop micro-XRF. *Spectrochim. Acta Part B At. Spectrosc.* 189, 106366. doi:10.1016/j.sab.2022.106366
- Wang, Z. Q., Chen, B., and Ma, X. H. (2014). Petrogenesis of the late Mesozoic Guposhan composite plutons from the nanling range, South China: Implications for W–Sn mineralization. *Am. J. Sci.* 314 (1), 235–277. doi:10.2475/01.2014.07
- Xiao, C. H., Chen, Z. L., Liu, X. C., Wei, C. S., Wu, Y., Tang, Y. W., et al. (2022). Structural analysis, mineralogy, and cassiterite U–Pb ages of the Wuxu Sb–Zn–polymetallic district, Danchi Fold-and-Thrust belt, South China. *Ore Geol. Rev.* 150, 105150. doi:10.1016/j.oregeorev.2022.105150
- Xiao, C. H., Shen, Y. K., and Wei, C. S. (2019). Petrogenesis of low Sr and high Yb A-type granitoids in the xianghualing Sn polymetallic deposit, south China: Constrains from geochronology and Sr–Nd–Pb–Hf isotopes. *Minerals* 9 (3), 182. doi:10.3390/min9030182
- Xiao, R., Li, X. F., Feng, Z. H., Yang, F., and Song, C. A. (2011). ⁴⁰Ar–³⁹Ar dating of muscovite from tungsten-quartz veins in Shanlu tungsten-tin deposit and its geological significance. *Min. Depos.* 30, 488–496. (in Chinese with English abstract). doi:10.16111/j.0258-7106.2011.03.010

- Xu, C. H., Zhang, L., Shi, H. S., Brix, M., Huhma, H., Chen, L. H., et al. (2017). Tracing an early jurassic magmatic arc from south to east China seas. *Tectonics* 36 (3), 466–492. doi:10.1002/2016TC004446
- Yang, F., Santosh, M., Kim, S. W., Zhou, H., and Jeong, Y. J. (2020). Late mesozoic intraplate rhyolitic volcanism in the north China craton: Far-field effect of the westward subduction of the Paleo-Pacific plate. *GSA Bull.* 132, 291–309. doi:10.1130/B35123.1
- Yang, J. H., Zhang, J. H., Chen, J. Y., and Sun, J. F. (2021). Mesozoic continental crustal rejuvenation of South China: Insights from zircon Hf-O isotopes of early Jurassic gabbros, syenites and A-type granites. *Lithos* 402–403, 105678–106403. doi:10.1016/j.lithos.2020.105678
- Yuan, S. D., Peng, J. T., Hu, R. Z., Bi, X. W., Qi, L., Li, Z. L., et al. (2008). Characteristics of rare-earth elements (REE), strontium and neodymium isotopes in hydrothermal fluorites from the Bailashui tin deposit in the Furong ore field, southern Hunan Province, China. *Chin. J. Geochem.* 27 (4), 342–350. doi:10.1007/s11631-008-0342-5
- Zaw, K., Peters, S. G., Cromie, P., Burrett, C., and Hou, Z. (2007). Nature, diversity of deposit types and metallogenic relations of South China. *Ore Geol. Rev.* 31 (1–4), 3–47. doi:10.1016/j.oregeorev.2005.10.006
- Zhang, D., Zhao, K. D., Wang, B. D., Cheng, K. D., Luo, X. L., Zhang, W., et al. (2020). Cretaceous granitic magmatism and mineralization in the Shanhu W-Sn ore deposit in the Nanling Range in South China. *Ore Geol. Rev.* 126, 103758. doi:10.1016/j.oregeorev.2020.103758
- Zhang, R. Q., Lu, J. J., Wang, R. C., Yang, P., Zhu, J. C., Yao, Y., et al. (2015). Constraints of *in situ* zircon and cassiterite U-Pb, molybdenite Re-Os and muscovite ⁴⁰Ar-³⁹Ar ages on multiple generations of granitic magmatism and related W-Sn mineralization in the wangxianling area, nanling range, south China. *Ore Geol. Rev.* 65, 1021–1042. doi:10.1016/j.oregeorev.2014.09.021
- Zhao, K. D., Jiang, S. Y., Zhu, J. C., Li, L., Dai, B. Z., Jiang, Y. H., et al. (2010). Hf isotopic composition of zircons from the Huashan-Guposhan intrusive complex and their mafic enclaves in northeastern Guangxi: Implication for petrogenesis. *Chin. Sci. Bull.* 55 (06), 509–519. doi:10.1007/s11434-009-0314-0
- Zhou, X. M., and Li, W. X. (2000). Origin of Late Mesozoic igneous rocks in southeastern China: Implications for lithosphere subduction and underplating of mafic magmas. *Tectonophysics* 326 (3–4), 269–287. doi:10.1016/S0040-1951(00)00120-7
- Zhou, X. M., Sun, T., Shen, W., Shu, L., and Niu, Y. (2006). Petrogenesis of mesozoic granitoids and volcanic rocks in south China: a response to tectonic evolution. *Episodes* 29 (1), 26–33. doi:10.18814/epiugs/2006/v29i1/004
- Zhu, J. C., Zhang, H., Xie, C. F., Zhang, P. H., and Yang, C. (2005). Zircon SHRIMP U-Pb geochronology, petrology and geochemistry of the Zhujianshui granite, Qitianling pluton, southern Hunan province. *Geol. J. China Univ.* 11, 335–342. Available at: <https://geology.nju.edu.cn/EN/Y2005/V11/I3/335> (in Chinese with English abstract).
- Zhu, J. C., Zhang, P. H., Xie, C. F., Zhang, H., and Yang, C. (2006). The huashan-guposhan A-type granitoid belt in the western part of the nanling mountains: petrology, geochemistry and genetic interpretations. *Acta Geol. Sin.* 04, 529–542. (in Chinese with English abstract).